Axon collateral pattern of a sparse locus coeruleus norepinephrine neuron in mouse cerebral cortex.

Running title: Axon Collaterals of the LC-NE Projection to the Cortex

Yu-Ming Wu[1,3], Wei-Chen Hung[1], Yun Chang[1,3], Ming-Yuan Min[1,2,*], Hsiu-Wen Yang[3,4,*].

[1]Department of Life Science, College of Life Science, National Taiwan University, Taipei 10617, Taiwan.
[2]Neurobiology and Cognitive Science Center, National Taiwan University, Taipei 10617, Taiwan.
[3]Department of Biomedical Sciences, Chung-Shan Medical University, Taichung 40201, Taiwan.
[4]Department of Medical Research, Chung-Shan Medical University Hospital, Taichung 40201, Taiwan.

***Correspondence:** mymin@ntu.edu.tw; hwy@csmu.edu.tw

Acknowledgments: We thank the Technology Commons, College of Life Science, National Taiwan University for technical support.

Funding: This work was supported by the National Science and Technology Council, Taiwan [Grant No: 111-2320-B-002 -015 -MY3 (MMY) and 113-2320-B-040-021-MY3 (HWY)].

Authors' contributions: YMW, performed the experiments and collected the data. HCW and YC assisted in data analysis. HWY and MYM designed the experiments and drafted the manuscript.

Data availability statement: All data supporting the results of this study are available from the corresponding authors upon reasonable request.

Declaration of interests: The authors report no competing interests.

Abstract

The locus coeruleus (LC) contains predominantly norepinephrine (NE) neurons with widespread axonal projections throughout the brain and plays a critical role in the control of behavior, particularly arousal. Historically, the LC-NE system was thought to perform this function by releasing NE uniformly throughout most brain regions. However, recent evidence suggests that the cortical projections of the LC are modularly organized, allowing coordination of diverse and sometimes opposing functions, such as fear memory formation and extinction. However, many details remain unclear, and answers require data from axon collaterals of sparse neurons. We modified a viral tracing protocol using a dual recombinase system to trace the axonal collaterals of sparse LC neurons projecting to the cingulate cortex (CgC). Our results show that even a small number of LC neurons still have broad cortical projections, but the pattern is not uniform. There are a few major projections with dense fibers and numerous minor projections with sparse innervation. Notably, the major projections, including the rostrosplenial cortex, dorsal hippocampus, somatosensory cortex, and CgC (the injection site for retrograde viral labeling), are functionally related and may coordinate goal-directed navigation. In conclusion, our results suggest that a single LC neuron projects divergently and non-uniformly to the cortex, with major projections coordinating related cortical areas to regulate specific functions, while minor

projections appear less functionally specific. It's likely that each LC-NE neuron plays a role in maintaining arousal through the minor projections.

Introduction

The locus coeruleus (LC) primarily consists of norepinephrine (NE) neurons. With widespread projections throughout the central nervous system, the LC serves as the brain and spinal cord's primary NE source (Schwarz et al., 2015; Aston-Jones and Waterhouse, 2016) and plays a key role in behavioral control (Aston-Jones and Cohen, 2005; Bouret and Sara, 2005; Sales et al., 2019; Poe et al., 2020). LC-NE activity strongly modulates arousal (McCarley and Hobson, 1975; Aston-Jones and Bloom, 1981; Takahashi et al., 2010; Carter et al., 2010; Joshi et al., 2016; Lovett-Barron et al., 2017; Breton-Provencher and Sur, 2019; Hayat et al., 2020), with low firing rates linked to sleep, moderate rates to alertness, and high rates to hyperactivity, attention deficits, and anxiety (Aston-Jones and Cohen, 2005). Traditionally, LC-NE neurons were thought to perform such function via a uniform NE projection to the cortex (Morrison et al., 1978; Biegon and Rainbow, 1983; Audet et al., 1988), enabling widespread NE release to influence entire neural networks in the cerebral cortex simultaneously (Poe et al., 2020). However, this view has been challenged by recent findings on LC's fiber pattern in the cortex and its functional role in behavioral regulation (Hansen and Manahan-Vaughan, 2015; Uematsu et al., 2017; Hirschberg et al., 2017; Takeuchi et al., 2016; McCall et al., 2017; Poe et al., 2020).

Quantitative analyses reveal that NE innervation is regionally specific rather than uniform, with denser NE fibers in the prefrontal cortex than in motor, somatosensory, and piriform cortices (Agster et al., 2013). Moreover, trans-synaptic pseudorabies virus tracing indicates that LC-NE neurons exhibit varying specificity in subcircuits (Schwarz et al., 2015). Retrograde viral tracing of axonal branches to the medial prefrontal cortex (mPFC) and primary motor cortex (M1) further suggests distinct patterns of axon collateralization (Plummer et al., 2020). These findings align with functional studies showing that LC-NE subcircuits orchestrate opposing learning states, facilitatory and extinctive fear learning via distinct amygdala- and mPFC-projecting modules (Uematsu et al., 2017). Likewise, a spinal-projecting module promotes analgesia in acute pain, whereas a prefrontal-projecting module generates aversion in chronic pain (Hirschberg et al., 2017). In summary, the LC-to-cortex projection is highly structured into functional modules. Understanding this modular arrangement, referred to as the LC-to-cortex module (LCCM), offers insights into how the LC-NE system regulates multiple functions, ensuring adaptive responses and behavioral flexibility.

However, details about LC-NE organization remain unclear. Specifically, it is uncertain whether an LCCM, such as the LC-mPFC module, consists of many LC-NE neurons with similar axon collateralization or if individual neurons exhibit distinct

patterns. Addressing this requires reducing labeled LC-NE neurons to single digits or even one neuron. This study aims to achieve that using the modified Tracing Axon Collaterals (TrAC) method (Plummer et al., 2020). The cingulate cortex (CgC) of the mPFC was targeted for retrograde virus tracing due to its critical role in emotional and cognitive functions (O'Doherty et al., 2002; Ito et al., 2003; Sanfey et al., 2003; Walton et al., 2007; Rolls, 2023), its highest NE fiber density among cortical areas (Agster et al., 2013; Schwarz et al., 2015; Plummer et al., 2020), and its function is largely modulated by the LC-NE system to perform complicated test behaviors such as go/no-go (Bourate and Sara, 2005) and two-alternative forced-choice (2-AFC; Aston-Jones and Cohen, 2005) tests. We found that even a few LC neurons project broadly across the cortex, but the pattern is not uniform, with major and minor projections. The major projections coordinate functionally related cortical areas, while minor projections, less functionally specific, likely contribute to general arousal maintenance throughout the brain.

Materials and Methods

Experiment Design for Tracing Axonal Collaterals of Sparse LC-NE Neurons

The TrAC method described by Plummer et al. (2020) effectively traces complete

axonal collaterals of LC-NE neurons. However, labeling too many neurons (up to hundreds) in a single experiment may obscure parts of their axonal collaterals due to overlap, leading to information loss. The TrAC method primarily uses a mouse strain carrying a dual recombinase-responsive fluorescent tracer (FT) allele crossed with a dopamine beta-hydroxylase (DBH), a synthesizing enzyme of NE and therefore a maker of NE neurons, -Flp mouse strain. This ensures NE neurons in the offspring express both Flp and the FT allele. A second recombinase, Cre, is introduced into a subset of LC-NE neurons projecting to the cortical area of interest via retrograde canine virus infusion. This process activates FT expression, allowing the entire axonal collaterals of all labeled LC-NE neurons to be visualized.

The number of labeled neurons depends on the amount of retrograde virus infused into the cortex and the viral vector's infection efficiency. Since viral transfection rates are typically below 100%, we refined this approach using dual AAV infusions while maintaining genetic specificity with dual recombinase-dependent FT expression. Specifically, we used tyrosine hydroxylase (TH), which is a marker for NE neurons due to its role as the rate-limiting enzyme for NE synthesis, -Cre mice (strain #: 025614, Jackson Laboratory), where the TH promoter drives Cre expression. We labeled a subset of LC-NE neurons projecting to the right CgC by infusing rAAV for Cre-

dependent Flp expression into the cortical region (Figure 1A). Instead of tracking all retrogradely labeled LC-NE neurons as in the original TrAC method, we traced a smaller subset by infusing AAV for Flp-dependent GCaMP6s expression (as FT) into the bilateral LC (Figure 1B). This dual AAV injection strategy successfully labeled sparse LC-NE neurons, enabling detailed tracing of their axonal collaterals.

Animals and stereotactic surgery for viral vector injection

Mice of both sexes were used in all experiments. They were housed and maintained in a temperature-controlled vivarium under a 12-hour light/dark cycle, with food and water available *ad libitum*. All animal experiments were approved by the Institutional Animal Care and Use Committees of NTU & CSMU, and every effort was made to minimize the number of animals used and their suffering. For stereotaxic surgery, mice aged 4-6 weeks were deeply anesthetized, as indicated by the absence of the hind paw withdrawal reflex, with an intraperitoneal injection of a mixture of zoletil (25 mg/kg) and xylazine hydrochloride (15 mg/kg); additional anesthetic doses were administered as required. Animals were then mounted in a stereotaxic apparatus, a small craniotomy was made over the right CgC, and the dura was reflected. A glass pipette loaded with AAV1-Syn-ChrisomR-tdT (marker AAV; addgene, Cat. No. 105714) to mark the cortical injection site and retrograde AAV-pEF1a-DIO-FLPo-WPRE-hGHpA

(rAAV; addgene, Cat. No. 105714) (ratio: marker AAV to rAAV = 1:2) was then slowly advanced into the right CgC using the coordinates (in mm): 1.0 caudal, 0.5 lateral, and 0.8 dorsal to the bregma. A total volume of 100 nl of AAV at a titer greater than $1x10^{13}$ was slowly infused. One week later, mice were again subjected to the same surgical procedures for stereotactic infusion of 100 nl of AAV8-Ef1a-fDIO-GCaMP6s (addgene, Cat. No. 105714) at a titer greater than $1x10^{13}$ into the bilateral LC using the following coordinates (in mm): -5.4 caudal, ±0.8 lateral, and 3.0 dorsal to the lambda. Both sets of coordinates for the CgC and LC were determined according to the Allen Brain Atlas. The tip of the glass pipette was bevelled to an angle of ~40° with a tip opening of 60-80 µm using a microelectrode beveler (BV-10, Sutter Instrument, Novato CA, USA) and connected to a 2.0 µL Hamilton syringe (Neuros Model 7002 KH, Hamilton, Reno, NV, USA). AAV was delivered manually at a rate of 5 nL/min.

Perfusion, Sections and IHC

Mice were deeply anesthetized with urethane (1.3 g/kg) and perfused via the cardiovascular system with 4% paraformaldehyde in 0.1 M phosphate buffer (PB). The brain was dissected and postfixed in the same fixative overnight at 4°C. After fixation, the brain was blocked into forebrain and brainstem (Fig. 1C). The brainstem was cut into 70 µm thick sections in the coronal plane using a vibratome (Lieca VT1000 S,

Germany), and serial sections containing the LC were collected and stained with antibodies against TH. The experiment was continued only if TH antibody staining showed that the number of labeled LC-NE neurons in the bilateral LC was less than a single digit and all labeled neurons showed TH-immunoreactivity (IR). In this case, the entire forebrain was sectioned with a vibratome into 70 μm thick sections in the coronal plane, and every third section of the entire consecutive forebrain sections was stained with IHC and examined (Figure 1C). Of these, those covering the CgC were stained by IHC with primary antibodies against TH and GCaMP6s (GFP) labeled with secondary antibodies conjugated to fluorophores with broad absorption/emission spectra. This fluorescence IHC (FIHC) staining was used to validate the viral infusion site showing tdtomato signal (marker AAV) and to confirm that GFP-IR fibers also showed TH-IR and thus originated from the LC. If any GFP-IR fibers were found that did not show TH-IR, the experiment was terminated. The remaining sections were stained with the primary antibodies against GFP alone, followed by staining with biotinylated secondary antibodies and avidin-biotin complex (ABC; VECTASTAIN® Elite® ABC Universal PLUS Kit); IR products were visualized using 3,3'-diaminobenzidine (DAB) as chromogen. After IHC, FIHC sections were stained with fluorescent Nissl; sections stained with IHC combined with the ABC (IHC/ABC) method and those not used for IHC were stained with conventional Nissl to facilitate identification of cortical regions.

For FIHC, sections were rinsed briefly with PB followed by phosphate-buffered saline (PBS; 0.9% NaCl in PB). Sections were incubated for 1 hour with a solution consisting of 10% normal goat serum (NGS) and 0.1% bovine serum albumin (BSA) in PBST (0.3% Triton in PBS) to block nonspecific reactions, followed by an additional 1-hour incubation with 0.05% thimerosal and 0.01% sodium azide in PBST for antigen retrieval. Sections were then incubated overnight at 4°C in a primary antibody cocktail including rabbit anti-TH (1:500 dilution; Cat. No. 6A2907, Merck Millipore, Burlington, MA, USA) and chicken anti-GFP (1:1000 dilution; Cat. No. ab13970, Abcam Inc., Cambridge, UK). For sections covering the CgC, the tdtomato (ChrisomR-tdT) signal was detected directly without further antibody staining. Sections were then incubated with a secondary antibody cocktail including goat anti-rabbit IgG conjugated to Alexa-594 (1:500 dilutions; Cat. No. A-11012, Thermo Fisher Scientific, Waltham, MA, USA) and goat anti-chicken IgY conjugated to CF®488A (1:1000 dilution; Cat. No. Biotium#20020, Biotium, Fremont, CA, USA) in PBST for 2 hours. Sections were washed three times for 10 minutes with PBST between antibody incubations. For the IHC/ABC method, the incubation of primary antibody was the same as described in FIHC, except that the sections were first treated with 3% H_2O_2 in 0.1 M PB for 20 minutes to quench endogenous peroxidase activity, followed by rinsing in 0.1 M PB and PBST, and the same chicken anti-GFP antibodies were used alone. After washing in PBST, sections

were incubated with biotinylated goat anti-chicken IgY secondary antibody (1:200 dilution; Cat. No. BA-9010; VectorLabs, Burlingame, CA, USA) in PBST for 1 hour, followed by washing in PBST and incubation with avidin-biotin-horseradish peroxidase complex (VECTASTAIN® Elite® ABC Universal PLUS Kit; VectorLabs) for 1 hour. After three washes with PBST and 0.1 M PB, sections were immersed in 0.05% DAB solution for 10 minutes, 0.004% H_2O_2 was added, and sections were incubated for an additional 10 minutes.

Data Analysis

After completion of the staining procedures, sections containing CgC were examined and photographed using a Zeiss LSM 780 confocal microscope system (Carl Zeiss); the other sections were examined and photographed using a light microscope system (Zeiss axio observer Z1 with Zen blue 3.1 software). For each section, images of the entire section were taken. The NE fibers and the outlines and landmarks of the section were traced using ImageJ software. The cortical areas constituting the section were identified by Nissl method with QuickNII software. The lengths of the traced NE fibers were measured and a histogram of ratio of total NE fiber length in a given area to that of the entre cortex was plotted (Figure 4B and Figure 5).

Results

CgC-projecting NE neurons appear to be randomly distributed in the LC

After a series of proof-of-concept experiments, we found that the time interval of 1 week between the infusion of rAAV (together with the marker AAV for the expression of tdtomato to mark the cortical injection site) into the CgC and AAV8 for the Flp-dependent expression of GCaMP6s into the LC, as well as the optimal survival time of 10 weeks after the AAV8 infusion, allowed the best results (Figure 1C). Notably, we found no NE fibers in the cortex with a survival time of less than 8 weeks after AAV8 infusion, although neurons with TH-IR were observed in the LC. Accordingly, we performed 10 experiments using the protocol described above (Figure 1C). Examination of LC sections stained with anti-TH antibody revealed that most of the GCaMP6s (GFP)-positive neurons also exhibited TH-IR in the LC, hereafter referred to as NE neurons, in 5 cases. The other 5 cases failed for unknown reasons because no NE neurons were found in the LC. Of the 5 successful cases, 40 NE neurons were labeled in one case, 5 NE neurons plus one neuron showing no TH-IR were labeled in one case, 5 NE neurons were labeled in two cases, and even better, a single NE neuron was labeled in one case (Figure 2A) in the LC ipsilateral to the cortical injection site. When the location of the 61 NE neurons from the 5 cases was constructed with registration according to the 4th ventricle using QuickNII software, it appears that these projection neurons to the CgC were randomly distributed rather than clustered

at a specific location in the LC (Figure 2B). This observation suggests that NE neurons projecting to the CgC do not have a specific topographical location in the LC, an observation consistent with that of Uematsu et al. (2017). Notably, there were also labeled LC-NE neurons in the contralateral LC; the total number of labeled neurons from the 5 cases is 8 cells, and again they appear to be randomly distributed in the contralateral LC (Figure 2B).

LC-NE neurons projecting to the mPFC show a feature of lateralized projection

We further quantitatively analyzed forebrain sections covering the CgC from the 3 cases, designated as Mouse# 513, Mouse# 543, and Mouse# 544 in which only 5 (2 cases) and 1 NE neuron (one case) were identified in the ipsilateral LC. The remaining 2 cases were not further investigated due to too many labeled cells (40) and the presence of a cell that did not show TH-IR in the ipsilateral LC. We confirmed that the examined GFP-IR fibers at the infusion site showed TH-IR (Figure 3A, B), hence GFP-IR, hereafter referred to as NE fibers. Interestingly, NE fibers were mostly found in the cortical areas and hippocampus ipsilateral to the injection side, while very rarely in the contralateral side (Figure 3C; Supplementary Figures 1-3). This observation suggests that although unilateral CgC infusion of rAAV labeled NE neurons on both sides of the LC, these labeled LC-NE neurons appear to have a lateralized projection to the cortex

and hippocampus; a similar result has been reported for LC-NE neurons projecting to the spinal cord (Hirschberg et al. 2017). Accordingly, we focused on a quantitative analysis of NE fiber distribution in the right cortex.

Axon projection from sparse LC-NE neurons to the cortex is divergent but not uniform

Upon completion of axon tracing in all examined forebrain sections, the lengths of traced NE fibers were measured, and a histogram of the ratio of total NE fiber length in a cortical region to that of the entire cortex (region-to-total fiber length ratio; RTFLR) was plotted. Interestingly, the results show that the distribution of NE fibers from even a handful of LC-NE neurons is still divergent and spans many cortical regions rather than being restricted to a few specific regions (Figure 4C, Supplementary Figures 1-3; Supplementary Table 1). However, the pattern is not uniform and includes a few cortical regions with fiber densities higher than or approximately equal to CgC (see asterisk in Figure 4) and more regions with much lower densities (see octothorpe in Figure 4). Theoretically, LC-NE neurons were labeled by the rAAV because they have a relatively large number of axonal projections to the CgC. Accordingly, we consider cortical regions with NE fiber densities similar to or even higher than the CgC to be the major cortical projections (MjCPs) of the retrogradely labeled LC-NE neurons, while the remaining areas with apparently lower densities are their minor cortical

projections (MiCPs). Since such a divergent but nonuniform pattern of cortical projection of sparse LC-NE neurons described above is applicable to all three study cases, we further investigate the functional implication of LC-NE neuron projection to the cortex according to this principle (see red lines in Figures 4 and 5).

The major projection targets of sparse LC-NE neurons in the cortex are functionally corelated

Figure 4B shows the NE fiber distribution of mouse #543, the core injection site in this case is at approximately Bregma 0.66 and covers mostly the CgC of the mPFC and a smaller portion in motor cortex 2 (see asterisk in Figure 3A1 and yellow shadow in Supplementary Figure 2). Five NE neurons are labeled in the ipsilateral LC and none in the contralateral LC (see blue circle in Figure 2B). As can be seen, despite the fact that the total number of labeled neurons is as low as 5 cells, the NE fiber distribution in the cortex is divergent but not uniform. In this case, the RTFLRs in somatosensory cortex 1 (S1), motor cortex 1 (M1), and motor cortex 2 (M2) are approximately equal to or slightly lower than those in the infusion site (the CgC). Notably, the RTFLRs in these cortical regions (including the CgC) are evidently higher than those in all other regions (as indicated by the red dashed line in Figure 4B), with the exception of the retrosplenial cortex (RSC), the dorsal hippocampal cortex (DHpc). In the RSC and DHpc,

the RTFLRs are higher than half of the CC and again apparently higher than in all other areas. Furthermore, it should be emphasized that all DHpc regions, including CA1, CA3, and the dentate gyrus (DG), have approximately the same the RTFLRs; in contrast, rare NE fibers were found in the ventral hippocampal cortex (VHpc). Thus, in this case, CgC, S1, M1, M2, RSC and DHpc are considered as MjCPs, while the others are considered as MiCPs. Regarding the functional correlations, we hypothesize that the labeled LC-NE neurons (or LCCMs) with the MjCPs may be involved in optimizing goal-directed navigation. We speculate that the modules may help the S1 to detect and process the salient stimulus in the environment, the CgC, which is involved in cognitive control, attention, emotion regulation, and decision making, to resolve conflicts in tasks involving uncertainty or error correction (O'Doherty et al., 2002; Sanfey et al., 2003; Walton et al., 2007; Joshi et al., 2016; Rolls, 2023), and the M1 and M2 to initiate the adaptive motor responses. Furthermore, since the DHpc is heavily involved in spatial memory and navigation (Strange et al., 2024), and the RSC is involved in spatial orientation, especially when integrating environmental memory with ongoing spatial experience (Vann et al., 2009; Mitchell et al., 2018; Alexander et al., 2023), the additional labeling of these two regions further supports our argument that the tagged LCCMs optimize goal-directed navigation by coordinating sensory, motor, and spatial memory information to guide adaptive behavior and efficient navigation through the

environment.

In mouse #544, the core cortical injection site was also predominantly located in the CgC (approximately at Bregma 0.98; see yellow shadow in Supplementary Figure 3), and a single NE neuron was labeled in the ipsilateral LC, while 2 were labeled in the contralateral LC (red circle in Figure 2B). Although fewer NE neurons were labeled compared to mouse #543, the distribution of NE fibers across the cortex is again divergent. Again, in addition to the CgC, the S1, RSC, and DHpc are classified as MjCPs because their RTFLRs are higher than those of the CgC (Figure 5A). As can be seen, these elements of MjCPs are similar to those of mouse #543, except that no motor region is included, reflecting the fact that fewer NE neurons (or LCCMs) were labeled. Interestingly, in mouse #544, while the RTFLR of the VHpc is significantly lower and classified as a MiCP, the DHpc has a much higher RTFLR than the injection site (the CgC). Again, the remaining cortical regions, including the VHpc, have apparently lower RTFLRs and were classified as MiCPs.

In mouse #513, the core cortical injection site was also located in the anterior CgC (approximately at Bregma 0.26), with some extension into the M2 cortex (see yellow shadow in Supplementary Figure 1). In this case, 5 NE neurons were labeled in the

ipsilateral LC and 3 in the contralateral LC (see yellow circle in Figure 2B). Again, even when the total number of labeled NE neurons is less than a single digit, the NE fiber distribution across the cortex is divergent (Figure 5B). The histogram of RTFLR shows that cortical regions with a higher value than in the CgC include the RSC, DHpc, VHpc, S1 and S2 cortices, M2 cortex, and olfactory piriform cortex (PC). In addition, M1 and extrastriate visual area 2 (V2), although slightly less dense, have RTFLRs approximately equivalent to those of the CgC (as indicated by the red dashed line in Figure 5B). Thus, in the case of this study, these cortical areas are considered to be the MjCPs of labeled LC-NE neurons (or LCCMs), with the remainder considered to be the MiCPs. Note that the functionally correlated CgC, RSC, and DHpc for spatial cognition are again classified as MjCPs. In addition, reflecting the fact that more LC-NE neurons (or LCCMs) are labeled in this study case, many more cortical regions are also classified as MjCPs compared to the other two cases. However, these additional labeled LCCMPs are located in either sensory (S1, S2, V2, PC) or motor (M1, M2) regions. These features are consistent with the idea of functional correlation deduced from the results of the previous two cases, that the tagged LCCMs may be involved in optimizing goal-directed navigation. The argument is furthermore supported by averaging the RTFLRs of the 3 study cases (Figure 5C). Interestingly, an exception to the MjCP in mouse #513 is that VHpc is also classified as one of the MjCPs.

Since the cortical regions, CgC, RSC and DHpc implicated in spatial navigation (are constantly defined as MjCPs and the anterior nucleus and laterodorsal nucleus of the thalamus (LD/AN) are also key structures in this navigation network (Vann et al., 2009; Mitchell et al., 2018), we also analyzed the RTFLRs in these 2 thalamic nuclei. The results show that the labeled LC-NE neurons generally have divergent projections to the thalamus (Fig. 3C, Supplementary Figures 1-3); interestingly, in contrast to the cortex and hippocampus, the projection seems to be bilateral as shown in mice #543 and #544 (Supplementary Figures 2-3). Nevertheless, the RTFLRs of the LD/AN do not meet the criteria as one of the MjCPs (Figure 5A,B), except that of mouse #543 (Figure 4B).

Discussion

Technical considerations

This study modified the TrAC protocol of Plummer et al. (2020) for sparsely labeling LC-NE neurons, taking advantage of the fact that viral vectors typically do not achieve complete transfection. We hypothesized that injecting rAAV would selectively tag a subset of LC-NE neurons projecting to the CgC, followed by a second AAV for Flp-dependent GCaMP6s expression, further limiting the number of labeled neurons. The

goal was to achieve high specificity and sparse labeling to facilitate functional imaging. Our approach resulted in a 30% success rate (3 out of 10 experiments) in labeling fewer than 10 neurons, which is a significant step toward better visualization and understanding of LC-NE neuron projections.

GCaMP6s was selected as the FT due to its superior axonal transport properties, which allow future studies aiming for high-resolution imaging of neuronal activity coordinated by the LC-NE system. The use of a dual recombinase system ensured specificity, as GFP-IR fibers observed at the rAAV injection site also exhibited TH-IR, confirming their identity as noradrenergic fibers. This approach provides a cost-effective and accessible strategy, utilizing publicly available materials to advance the study of LC-NE neurons in behavioral and cognitive neuroscience.

A single LC-NE neuron may coordinate a specific brain function through MjCPs

Targeting the CgC for LC-NE labeling offers insight into how these LC-NE neurons orchestrate higher-order cognitive functions involving the CgC. Given the low transfection efficiency of AAV, we propose that the CgC should receive relatively high innervation, and brain areas that share similar NE fiber innervation, termed major cortical projection regions (MjCPs), are functionally co-activated by the labeled LC-NE

neurons during specific behaviors requiring attention, spatial navigation, and decision making.

The consistent MjCPs identified across our dataset, namely the CgC, RSC, and DHpc, align with established neural networks implicated in spatial navigation (Vann et al., 2009; Mitchell et al., 2018). These regions form key components of an interconnected system that supports spatial memory and cognitive mapping (Van Groen and Wyss, 1990, 1992, 2003; Jones et al., 2005; Kobayashi and Amaral, 2007). Although the LD/AN did not consistently meet MjCP criteria, their average RTFLR (Figure 5C) is the highest among MiCPs. Considering the very small area of the thalamic nuclei compared to the CgC, RSC and DHpc, the labeled LC-NE neurons could still effectively activate the LD/AN to interact with the other MjCPs. Our data further indicate that contralateral LC-NE neurons predominantly project contralaterally, while ipsilateral neurons project ipsilaterally, with potential decussation at the thalamic level. These findings refine our understanding of how LC-NE neurons contribute to network-wide coordination during goal-directed behaviors.

Mouse #544, which exhibited the sparsest labeling (one ipsilateral neuron, two contralateral neurons), demonstrated MjCPs that included the S1, suggesting an

involvement in attentional regulation. The RSC, known for relaying sensory input to the hippocampus (Vogt and Miller, 1983; Vann et al., 2009), further supports the notion that the labeled LC-NE neurons integrate sensory cues for navigation and decision-making. Together, the labeled LC-NE neurons in Mouse #544 s appear to form a functional module dedicated to task-specific processing. It also suggests the possibility that even a single LC-NE neuron may exert influence over multiple interconnected brain regions, as the number of MjCPs is greater than the number of labeled LC-NE neurons.

Mouse #543, in which five ipsilateral LC-NE neurons were labeled, showed a similar MjCP profile to mouse #544, but additionally included M1 and M2. This suggests that LC-NE activity in these regions supports sensorimotor integration (Alsene and Bakshi, 2011; Kuo et al., 2020), consistent with previous studies indicating that NE facilitates stimulus discrimination and motor execution. The co-labeling of these motor-associated cortical regions further highlights the role of LC-NE neurons in coordinating cognitive and motor functions, particularly in behaviors requiring fine-tuned attention and movement planning (Usher et al., 1999; Aston-Jones and Cohen, 2005). Mouse #513, which exhibited the most extensive labeling (five ipsilateral neurons, three contralateral neurons), had RTFLRs overlapping with previous cases but

additionally included sensory-associated areas such as PC, S2, and V2, as well as the VHpc. This suggests that a larger population of LC-NE neurons engages in broader functional coordination, potentially optimizing cognitive performance in more complex environments.

Taken together, our findings reinforce the idea that LC-NE neurons regulate a broad spectrum of cognitive functions, including spatial memory, sensory processing, and motor control. These neurons likely play a pivotal role in facilitating goal-directed navigation and adaptive decision-making. The presence of discrete noradrenergic neuron subpopulations with functionally correlated MjCPs suggests a highly modular organization within the LC, where even a single neuron may significantly influence neural network dynamics. This further implies that cortical and subcortical inputs selectively engage different LC projection modules to fine-tune behavioral responses in varying contexts.

All LC-NA neurons contribute to the maintenance of consciousness via MiCPs

In our study, MiCPs were widespread but had lower RTFLRs. Given the low RTFLRs, it is unlikely that a LC-NE neuron is labeled by rAAV infused into one of the MiCPs. Namely, the RTFLR patterns observed across different cases suggest that no single

neuron projects exclusively to MiCPs. Instead, the present results imply that the RTFLR pattern in each study case arises from the summation of labeled LC-NE neurons with distinct MjCPs and MiCPs, and supports a modular organization within the LC, where each functional module targets specific MjCPs while concurrently contributing to global arousal regulation through MiCPs. This modular arrangement allows LC-NE neurons to engage in distinct functions, such as modulating fear memory formation versus extinction (Uemasu et al., 2017) and pro-nociception *vs*. antinociception (Hirschberg et al., 2017), by selectively influencing target regions through synaptic NE release. At the same time, all LC-NE neurons contribute to overall arousal regulation via diffuse NE transmission within MiCPs. This dual mode of action, localized NE release for precise functional modulation and widespread NE diffusion for arousal, enables LC-NE neurons to flexibly coordinate cognitive and behavioral states. Electron microscopy studies suggest that NE exerts its effects through both synaptic and volumetric transmission mechanisms (Vizi et al., 2004; Min et al., 2007; Fuxe et al., 2015). Synaptic transmission enables high specificity in modulating processing within MjCPs, ensuring optimal neural function for task-relevant behaviors. In contrast, volume transmission supports a more diffuse and sustained influence across MiCPs, maintaining cognitive vigilance and attentional readiness. Future studies should explore the relative contributions of these transmission modalities across different

projection targets, potentially revealing novel mechanisms underlying LC-NE modulation of cognition and behavior.

Conclusions

Our study provides new insights into the cortical projections of LC-NE neurons labeled via rAAV infusion into the CgC. Key findings include: 1. CgC-projecting LC-NE neurons are randomly distributed throughout the LC, without a clear spatial clustering pattern. 2. The unilateral LC projects to both hemispheres, but individual LC-NE neurons exhibit lateralized, non-bidirectional projections. 3. Single LC-NE neurons display divergent but non-uniform projection patterns, characterized by dense MjCPs and sparse MiCPs. 4. MjCPs are functionally interconnected and contribute to specific cognitive and behavioral processes, such as spatial navigation, sensory-motor coordination, and attentional control.

These results suggest that individual LC-NE neurons serve as functional hubs, integrating multiple cortical regions to coordinate specific behaviors. Meanwhile, all LC-NE neurons collectively contribute to arousal regulation through widespread MiCP projections (see Figure 6). This modular organization within the LC provides a flexible mechanism for neural network coordination, allowing for adaptive behavioral

responses in complex environments. Further research is necessary to determine how different LC-NE neuron subtypes interact with distinct neural circuits and how these interactions shape cognition and behavior by revealing more single or sparse LC-NE neuron with rAVV infused to different cortical regions.

References

1. Agster KL, Mejias-Aponte CA, Clark BD, Waterhouse BD (2013). Evidence for a regional specificity in the density and distribution of noradrenergic varicosities in rat cortex. *J Comp Neurol* **521**, 2195–207.

2. Alexander AS, Place R, Starrett MJ, Chrastil ER, Nitz DA (2023). Rethinking retrosplenial cortex: Perspectives and predictions. *Neuron* **111**, 150-175.

3. Alsene KM and Bakshi VP (2011). Pharmacological stimulation of locus coeruleus reveals a new antipsychotic-responsive pathway for deficient sensorimotor gating. *Neuropsychopharmacology* **36**, 1656-67.

4. Aston-Jones G, Bloom FE (1981). Activity of norepinephrine-containing locus coeruleus neurons in behaving rats anticipates fluctuations in the sleep-waking cycle. *J Neurosci* **1**, 876-86.

5. Aston-Jones G, Cohen JD (2005). An integrative theory of locus coeruleus-

norepinephrine function: adaptive gain and optimal performance. *Annu Rev Neurosci* **28**, 403-50.

6. Aston-Jones G, Waterhouse BD (2016). Locus coeruleus: from global projection system to adaptive regulation of behavior. *Brain Res* **1465**, 75-8.

7. Audet MA, Doucet G, Oleskevich S, Descarries L (1988). Quantified regional and laminar distribution of the noradrenaline innervation in the anterior half of the adult rat cerebral cortex. *J Comp Neurol* **274**, 307-18.

8. Biegon A, Rainbow TC (1983). Localization and characterization of [3H]desmethylimipramine binding sites in rat brain by quantitative autoradiography. *J Neurosci* **3**, 1069-76.

9. Bouret S, Sara SJ (2005). Network reset: a simplified overarching theory of locus coeruleus noradrenaline function. *Trends Neurosci* **28**, 574-82.

10. Breton-Provencher V, Sur M (2019). Active control of arousal by a locus coeruleus GABAergic circuit. *Nat Neurosci* **22**, 218-28.

11. Carter ME, Yizhar O, Chikahisa S, Nguyen H, Adamantidis A, Nishino S, Deisseroth K, de Lecea L (2010). Tuning arousal with optogenetic modulation of locus coeruleus neurons. *Nat Neurosci* **13**, 1526-33.

12. Chandler DJ, Gao WJ, Waterhouse BD (2014). Heterogeneous organization of the

locus coeruleus projections to prefrontal and motor cortices. *Proc Natl Acad Sci USA* **111**, 6816-21.

13. Fuxe K, Agnati LF, Marcoli M, Borroto-Escuela DO (2015). Volume transmission in central dopamine and noradrenaline neurons and its astroglial targets. *Neurochem Res* **40**, 2600-14.

14. Hansen N, Manahan-Vaughan D (2015). Hippocampal long-term potentiation that is elicited by perforant path stimulation or that occurs in conjunction with spatial learning is tightly controlled by β-adrenoreceptors and the locus coeruleus. *Hippocampus* **25**, 1285-98.

15. Hayat H, Regev N, Matosevich N, Sales A, Paredes-Rodriguez E, Krom AJ, Bergman L, Li Y, Lavigne M, Kremer EJ, Yizhar O, Pickering AE, Nir Y (2020). Locus coeruleus norepinephrine activity mediates sensory-evoked awakenings from sleep. *Sci Adv* **6**, eaaz4232.

16. Hirschberg S, Li Y, Randall A, Kremer EJ, Pickering AE (2017). Functional dichotomy in spinal- vs prefrontal-projecting locus coeruleus modules splits descending noradrenergic analgesia from ascending aversion and anxiety in rats. *Elife* **6**, e29808.

17. Ito S, Stuphorn V, Brown JW, Schall JD (2003). Performance monitoring by the anterior cingulate cortex during saccade countermanding. *Science* **302**, 120 -22.

18. Jones BF, Groenewegen HJ, Witter MP (2005). Intrinsic connections of the cingulate cortex in the rat suggest the existence of multiple functionally segregated

networks. *Neuroscience* **133**, 193–207.

19. Joshi S, Li Y, Kalwani RM, Gold JI (2016). Relationships between pupil diameter and neuronal activity in the locus coeruleus, colliculi, and cingulate cortex. *Neuron* **89**, 221-34.
20. Kobayashi Y, Amaral DG (2007). Macaque monkey retrosplenial cortex: III. Cortical efferents *J Comp Neurol* **502**, 810-33.

21. Lovett-Barron M, Andalman AS, Allen WE, Vesuna S, Kauvar I, Burns VM, Deisseroth K (2017). Ancestral Circuits for the Coordinated Modulation of Brain State. *Cell* **171**, 1411-23.

22. McCall JG, Siuda ER, Bhatti DL, Lawson LA, McElligott ZA, Stuber GD, Bruchas MR (2017). Locus coeruleus to basolateral amygdala noradrenergic projections promote anxiety-like behavior. *Elife* 6, e18247.

23. McCarley RW, Hobson JA (1975) Neuronal excitability modulation over the sleep cycle: a structural and mathematical model. *Science* **189**, 58-60.

24. Min MY, Hsu PC, Lu HW, Lin CJ, Yang HW (2007). Postnatal development of noradrenergic terminals in the rat trigeminal motor nucleus: A light and electron microscopic immunocytochemical analysis. *Anat Rec* **290**, 96-107.

25. Mitchell AS, Czajkowski R, Zhang N, Jeffery K, Nelson AJD (2018). Retrosplenial cortex and its role in spatial cognition. *Brain Neurosci Adv* **2**, 2398212818757098.

26. Morrison JH, Grzanna R, Molliver ME, Coyle JT (1978). The distribution and orientation of noradrenergic fibers in neocortex of the rat: an immunofluorescence study. *J Comp Neurol* **181**, 17-39.

27. Mueller D, Porter JT, Quirk GJ (2008). Noradrenergic signaling in infralimbic cortex increases cell excitability and strengthens memory for fear extinction. *J Neurosci* **28**, 369-75.

28. O'Doherty JP, Deichmann R, Critchley HD, Dolan RJ (2002). Neural responses during anticipation of a primary taste reward. *Neuron* **33**, 815-26.

29. Poe GR, Foote S, Eschenko O, Johansen JP, Bouret S, Aston-Jones G, Harley CW, Manahan-Vaughan D, Weinshenker D, Valentino R, Berridge C, Chandler DJ, Waterhouse B, Sara SJ (2020). Locus coeruleus: a new look at the blue spot. *Nat Rev Neurosci* 21, 644-59.

30. Plummer NW, Chandler DJ, Powell JM, Scappini EL, Waterhouse BD, Jensen P (2020). An Intersectional Viral-Genetic Method for Fluorescent Tracing of Axon Collaterals Reveals Details of Noradrenergic Locus Coeruleus Structure. *eNeuro* **7**, ENEURO.0010-20.2020.

31. Roesch MR, Olson CR (2004) Neuronal activity related to reward value and motivation in primate frontal cortex. *Science* **304**, 307-10.

32. Rolls ET (2023). Emotion, motivation, decision-making, the orbitofrontal cortex, anterior cingulate cortex, and the amygdala. *Brain Struct Funct* **228,** 1201-1257.

33. Sales AC, Friston KJ, Jones MW, Pickering AE, Moran RJ (2019). Locus coeruleus tracking of prediction errors optimises cognitive flexibility: an active inference model. *PLoS Comput Biol* **15**, e1006267.

34. Sanfey AG, Rilling JK, Aronson JA, Nystrom LE, Cohen JD (2003). The neural basis of economic decision-making in the Ultimatum Game. *Science* **13**, 1755-8.

35. Schwarz LA, Miyamichi K, Gao XJ, Beier KT, Weissbourd B, DeLoach KE, Ren J, Ibanes S, Malenka RC, Kremer EJ, Luo L (2015). Viral-genetic tracing of the input-output organization of a central noradrenaline circuit. *Nature* **524**, 88-92.

36. Strange BA, Witter MP, Lein ES, Moser EI. Functional organization of the hippocampal longitudinal axis (2014). *Nat Rev Neurosci* **15**, 655-69.

37. Takahashi K, Kayama Y, Lin JS, Sakai K (2010). Locus coeruleus neuronal activity during the sleep-waking cycle in mice. *Neuroscience* **169**, 1115-26.

38. Takeuchi T, Duszkiewicz AJ, Sonneborn A, Spooner PA, Yamasaki M, Watanabe M, Smith CC, Fernández G, Deisseroth K, Greene RW, Morris RG (2016). Locus coeruleus and dopaminergic consolidation of everyday memory. *Nature* **537**, 357-62.

39. Uematsu A, Tan BZ, Ycu EA, Cuevas JS, Koivumaa J, Junyent F, Kremer EJ, Witten IB, Deisseroth K, Johansen JP (2017). Modular organization of the brainstem noradrenaline system coordinates opposing learning states. *Nat Neurosci* **20**, 1602-11.

40. Usher M, Cohen JD, Servan-Schreiber D, Rajkowski J, Aston-Jones G (1999). The role of locus coeruleus in regulation of cognitive performance. *Science* **283**, 549-54.

41. Van Groen T, Wyss J M (1990). Connections of the retrosplenial granular a cortex in the rat. *J Comp Neurol* **300**, 593-606.

42. Van Groen T, Wyss JM (1992). Connections of the retrosplenial dysgranular cortex in the rat. *J Comp Neurol* **315**, 200-16.

43. Van Groen T, Wyss JM (2003). Connections of the retrosplenial granular b cortex in the rat. *J Comp Neurol* **463**, 249–63.

44. Vann SD, Aggleton JP, Maguire EA (2009). What does the retrosplenial cortex do? *Nat Rev Neurosci* **10**, 792-802.

45. Vizi ES, Kiss JP, Lendvai B (2004). Nonsynaptic communication in the central nervous system. *Neurochem Int* **45**, 443–51.

46. Vogt BA, Miller MW (1983) Cortical connections between rat cingulate cortex and visual, motor, and postsubicular cortices. *J Comp Neurol* **216**, 192–210.

47. Walton ME, Croxson PL, Behrens TE, Kennerley SW, Rushworth MF (2007). Adaptive decision making and value in the anterior cingulate cortex. *Neuroimage*

Suppl 2, T142-54.

48. Zerbi V, Floriou-Servou A, Markicevic M, Vermeiren Y, Sturman O, Privitera M, von Ziegler L, Ferrari KD, Weber B, De Deyn PP, Wenderoth N, Bohacek J (2019). Rapid Reconfiguration of the Functional Connectome after Chemogenetic Locus Coeruleus Activation. *Neuron 103*, 702-18.

Figures and Legends

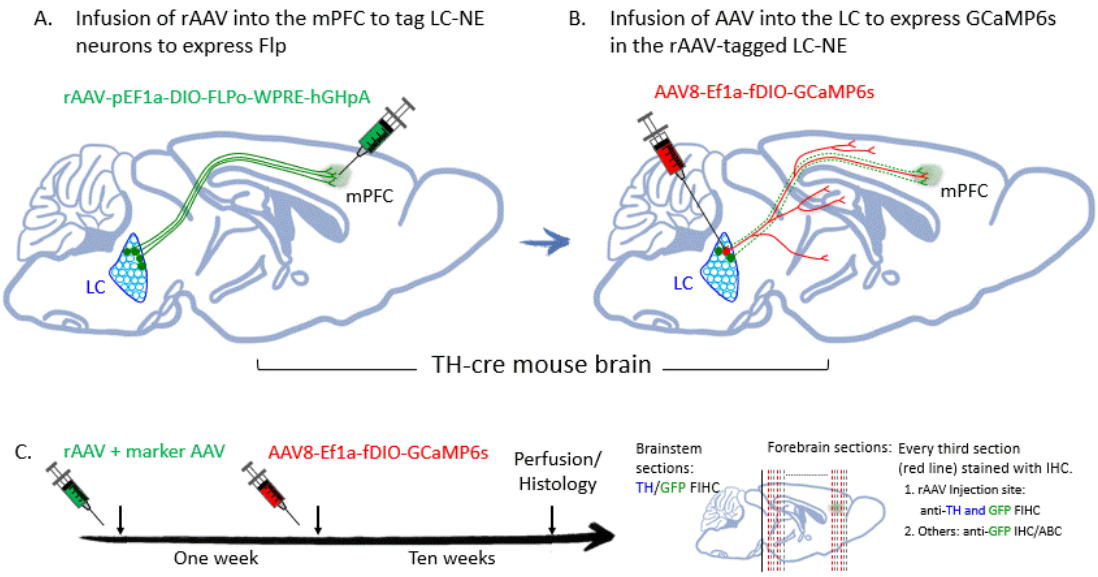

Figure 1. Modified TrAC to reveal whole axon collaterals of sparse LC-NE neurons. ***A***. Schematic illustration of retrograde AAV-mediated transduction of a subset of LC-NE neurons projecting to the CgC to express Flp. ***B***. Schematic illustrating the infusion of AAV into the LC to express GCaMP6s in a fraction of rAAV-tagged LC-NE projecting to the CgC. ***C***. Timeline of rAAV infusion into the CgC for Cre-dependent expression of Flp, AAV8 infusion into the LC for Flp-dependent expression of GCaMP6s and histological processing (left), and schematic illustrating block (thick line) of brain for brainstem and forebrain sectioning after perfusion and grouping of forebrain sections for IHCs and Nissl staining (right).

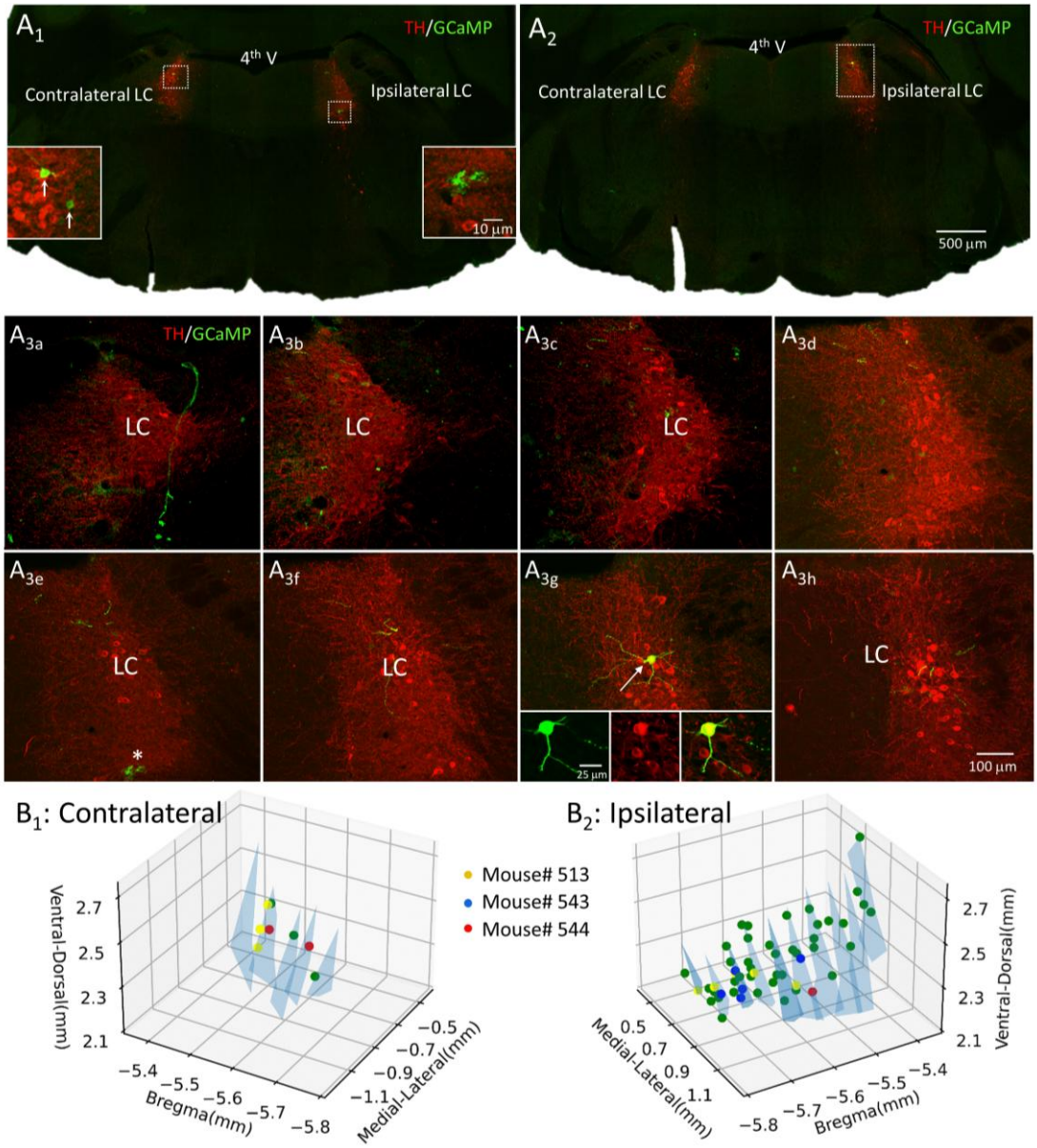

Figure 2. Representative result showing labeling of 3 NE neurons in bilateral LC using the modified TrAC method (data from mouse #544). ***A***. Two low-power images show IHC with primary antibodies against TH (red) and GFP (green). Two and one neurons are labeled in the LC contralateral (A1) and ipsilateral (a2) to the rAAV infusion site, respectively. The lower left inset in A1 is an enlargement of the dotted area of the contralateral LC and shows the two labeled neurons (arrows). Note that the structures in the dashed area of the ipsilateral LC are not neurons, as shown in the lower right inset. Eight high-power images (A3) show sections covering the entire ipsilateral LC; the section (A3g) showing the cell body and proximal dendrites of the labeled neuron is an enlargement of the dashed area shown in A2; also, the insets at the bottom show

the labeled neuron with TH-IR. ***B***. Distribution of all labeled NE (TH- and GFP-IR) neurons in the contralateral (B1) and ipsilateral LC (B2) summarized from the 5 study cases. Yellow, blue, and red circles denote data from mice #513, #543, and #544, respectively; green circle denotes data from the other 2 study cases. The light blue triangular shadow delineates the LC.

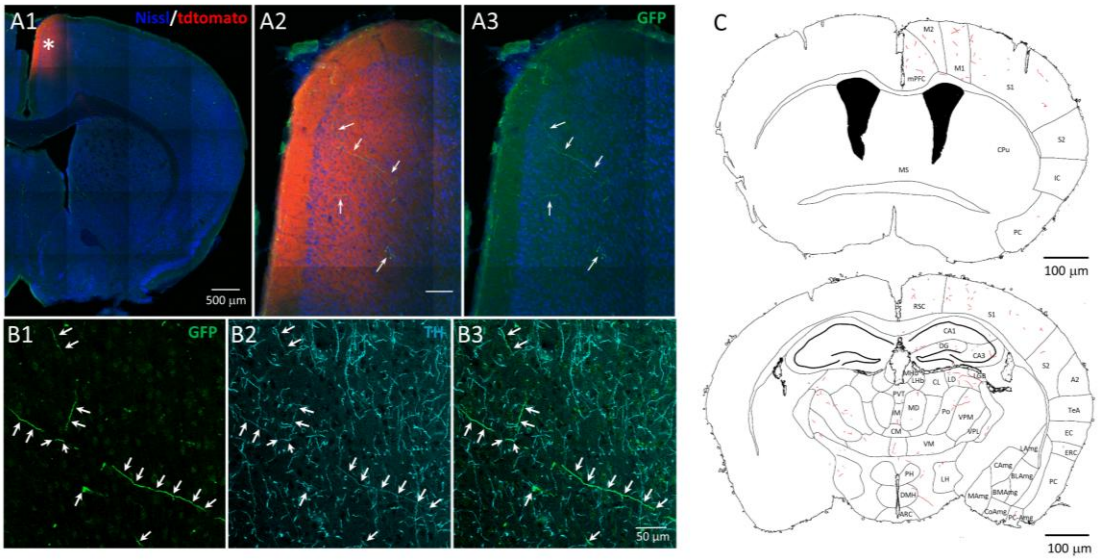

Figure 3. Representative result showing NE (TH and GFP-IR) axons traced in the CgC using the modified TrAC method (data from mouse #543). ***A***. Merged image of tomato (red), GFP (green) and Nissl (blue) staining of one of the forebrain sections covering the viral infusion site (asterisk in A1 marks the CgC). Magnification of the CgC (A2) shows GFP (GCaMP6s)-IR fibers as indicated by arrows. The fibers are better seen when the tdtomato signal is removed (A3). ***B***. Images show the same field from the next consecutive section stained with anti-GFP (GCaMP6s, gray in B1) and anti-TH (cyan in B2) antibodies and the merged image (B3). Note that all GFP (GCaMP6s)-IR fibers also exhibit TH-IR as indicated by the arrows. ***C***. Representative plots of complete tracking of NE fibers in 2 sections stained with IHC/ABC. Note the unilateral and bilateral distribution of NE fibers in the cortex and thalamus (bottom). *Brain region abbreviations*: **A2**: Secondary auditory cortex; **ARC**: arcuate area (of the hypothalamic area); **BLAmg**: Basolateral amygdala nucleus; **BMAmg**: Basomedial amygdala nucleus; **CA1**: Cornu ammonis area 1 (of the hippocampus); **CA3**: Cornu ammonis area 3 (of the hippocampus); **CAmg**: Central amygdala nucleus; **CL**: Centrolateral thalamic nucleus; **CM**: Centromedial thalamic nucleus; **CoAmg**: Cortical amygdala nucleus; **CPu**: Caudate putmen (striatum); **DG**: Dentate gyrus (of the hippocampus); **DMH**: Dorsomedial

hypothalamic area; **EC**: Ectorhinal cortex; **ERC**: Entorhinal cortex; **IC**: Insular cortex; **IM**: Intermedial thalamic nucleus; **LAmg**: Lateral amygdala nucleus; **LD**: Laterodorsal thalamic nucleus; **LGB**: lateral geniculate body; **LH**: Lateral hypothalamic area; **LHb**: Lateral habenular nucleus; **M1**: Primary motor cortex; **M2**: Secondary motor Cortex; **MAmg**: Medial amygdala nucleus; **MD**: Mediodorsal thalamic nucleus; **MHb**: Medial habenular nucleus; **mPFC**: Medial prefrontal cortex; **MS**: Medial septal nucleus; **PC**: Piliform cortex; **PCAmg**: Piriform-amygdala area; **PH**: Posterior hypothalamic area; **Po**: Posterior thalamic nucleus; **PVT**: Paraventricular thalamic nucleus; **RSC**: Retrosplenial cortex; **S1**: Primary somatosensory cortex; **S2**: Secondary somatosensory cortex; **TeA**: Temporal association cortex; **VM**: Ventromedial thalamic nucleus; **VPL**: Ventral posterolateral thalamic nucleus; **VPM**: Ventral posteromedial thalamic nucleus.

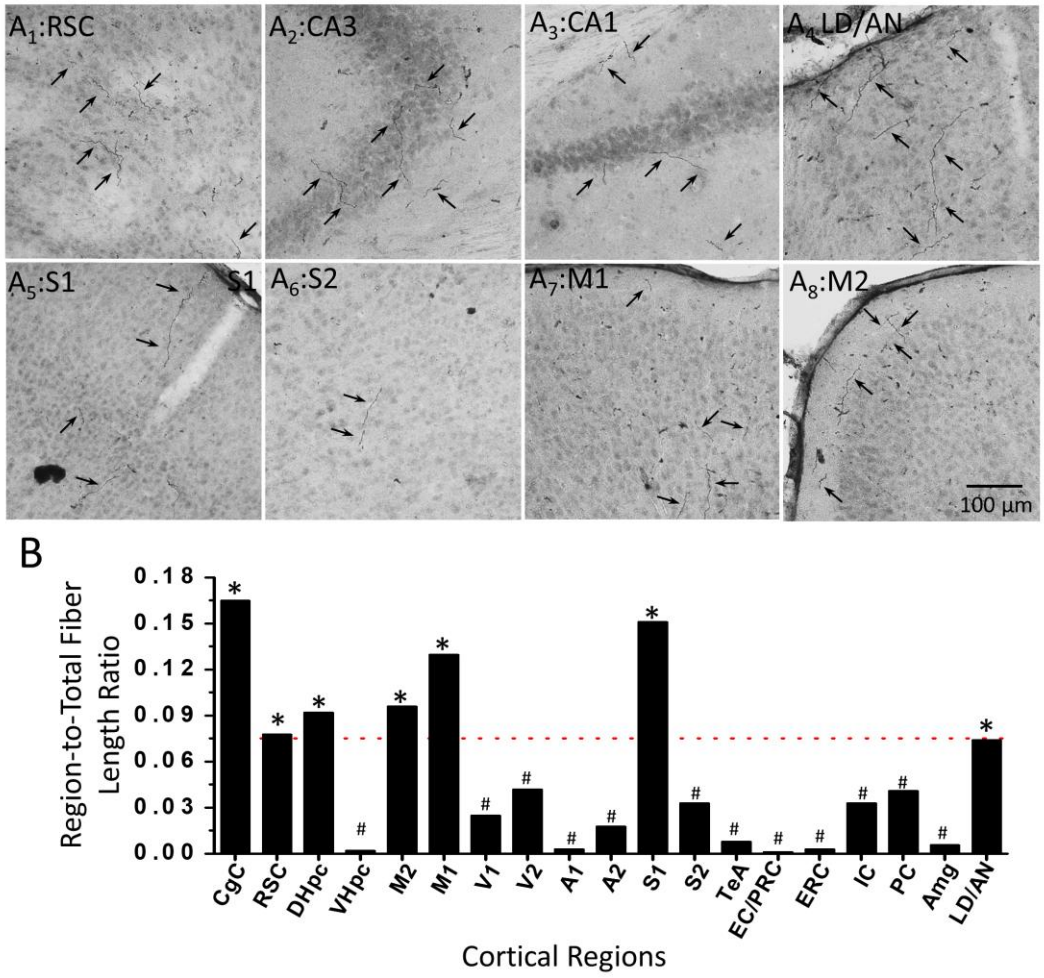

Figure 4. Representative result showing NE axon tracing in other cortical regions using the modified TrAC and anti-GFP IHC-ABC methods (data from mouse #543). ***A***. Representative images of sections not covering the CgC (rAAV infusion site) stained with anti-GFP IHC-ABC showing NE fibers in RSC (A1), CA3 (A2), CA1 (A3), DL/AN (A4), S1 (A5), S2 (A6), M1 (A7), M2 (A8). ***B***. RTFLR histogram of mouse #543. * denotes MjCPs and # denotes MiCPs. The red dotted line shows the separation of MjCPs and MiCPs. Cortical region abbreviations: **A1**: Primary auditory cortex; **A2**: Secondary auditory cortex; **Amg**: Amygdala; **AN**: anterior nucleus (of the thalamus); **CgC**: cingulate cortex; **DHpc**: Dorsal hippocampus; **EC/PRC**: Ectorhinal cortex/ perirhinal cortex; **ERC**, entorhinal cortex; **IC**: Insular cortex; **LD**: laterodorsal nucleus (of the thalamus); **M1**: Primary motor cortex; **M2**: secondary motor cortex; **PC**: Pontine cortex; **RSC**: retrosplenial cortex; **S1**: Primary somatosensory cortex; **S2**: Secondary somatosensory cortex; **TeA**: Temporal association area; **V1**: Primary visual cortex; **V2**: Secondary visual cortex; **VHpc**: Ventral hippocampus.

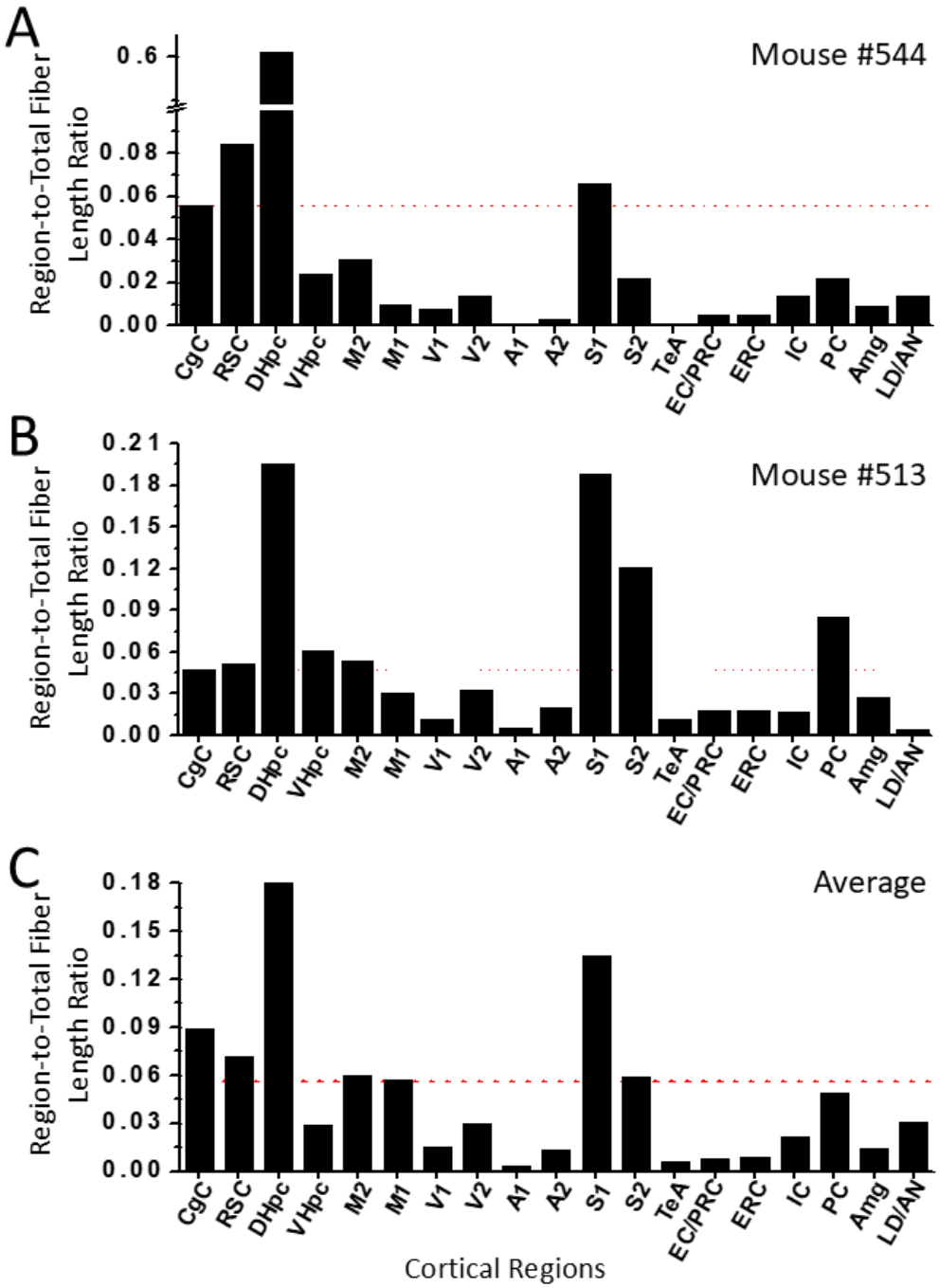

Figure 5. TFLR histograms of mouse #544 (***A***), mouse #513 (***B***) and the sum of the 3 study cases (***C***). The red dotted line shows the separation of MjCPs and MiCPs. See Figure 4 for *abbreviations* of cortical regions.

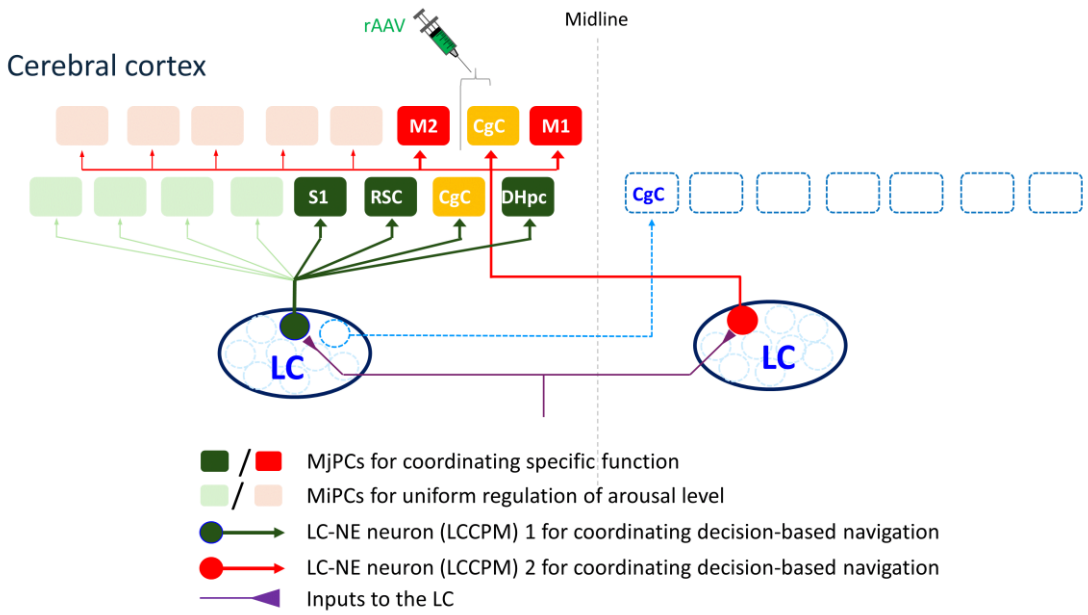

Figure 6. The graphical summary summarizes the conclusions (see the last paragraph of the Discussion).